Modeling the Impact of Convective Entrainment on the Tropical Tropopause

F. J. ROBINSON AND S. C. SHERWOOD

Department of Geology and Geophysics, Yale University, New Haven, Connecticut

(Manuscript received 29 November 2004, in final form 12 August 2005)

ABSTRACT

Simulations with the Weather Research and Forecasting (WRF) cloud-resolving model of deep moist convective events reveal net cooling near the tropopause (~15–18 km above ground), caused by a combination of large-scale ascent and small-scale cooling by the irreversible mixing of turbulent eddies overshooting their level of neutral buoyancy. The turbulent cooling occurred at all CAPE values investigated (local peak values ranging from 1900 to 3500 J kg^{-1}) and was robust to grid resolution, subgrid-scale turbulence parameterization, horizontal domain size, model dimension, and treatment of ice microphysics. The ratio of the maximum downward heat flux in the tropopause to the maximum tropospheric upward heat flux was close to 0.1. This value was independent of CAPE but was affected by changes in microphysics or subgrid-scale turbulence parameterization.

The convective cooling peaked roughly 1 km above the cold point in the background input sounding and the mean cloud- and (turbulent kinetic energy) TKE-top heights, which were all near 16.5 km above ground. It was associated with turbulent entrainment of stratospheric air from as high as 18.25 km into the troposphere. Typical cooling in the experiments was of order 1 K during convective events that produced order 10 mm of precipitation, which implied a significant contribution to the tropopause energy budget. Given the sharp concentration gradients and long residence times near the cold point, even such a small entrainment rate is likely consequential for the transport and ambient distribution of trace gases such as water vapor and ozone, and probably helps to explain the gradual increase of ozone typically observed below the tropical tropopause.

1. Introduction

Convective overturning mixes most of the tropical troposphere on a time scale of around a week or so. The tropopause refers to the atmospheric level at which rapid convective overturning ceases, yielding to the very nearly radiatively balanced stratosphere with its very slow diabatic overturning of a few years' time scale. However, it has become clear that the cessation of convective activity occurs gradually rather than all at once, and that a transition region known as the tropical tropopause layer (TTL) must be considered where convective effects remain but no longer dominate those of radiation and/or stratospheric overturning. This layer is typically taken to begin somewhere from 11–14 km and to extend at least to the cold point near 17–18 km in boreal winter, or even as high as 20–22 km, the altitude of the deepest well-documented convective storms (Simpson et al. 1993).

The temperature at the cold point (within the TTL) is important because it is thought to determine the amount of stratospheric water vapor and/or the prevalence of cirrus clouds in that region. As the upward arm of the Brewer–Dobson circulation goes through the TTL (returning at high latitudes) the cold point temperature sets the stratospheric entry humidity (Holton and Gettelman 2001). The air passing through the TTL is expected to be freeze dried to the saturation mixing ratio of the cold tropical tropopause (Hartmann et al. 2001). Further, because the horizontal velocities at those altitudes are 4 orders of magnitude greater than the vertical velocities, the properties of the air at other longitudes tends to be strongly linked to the cold point temperature (cold trap) in the Tropics (Fueglistaler et al. 2004). Thus, TTL temperatures in deeply convective regions carry disproportionate importance in regulating stratospheric water vapor.

Views have been mixed as to whether/how much tropospheric convection is able to affect the tropopause

Corresponding author address: F. J. Robinson, Dept. of Geology and Geophysics, Kline Geology Laboratory, P.O. Box 208109, Yale University, New Haven, CT 06520-8109.
E-mail: francis.robinson@yale.edu

layer. Some investigators have argued that the troposphere and temperature minimum are decoupled and that the TTL temperature is determined by stratospheric thermodynamics (Kirk-Davidoff et al. 1999; Küpper et al. 2004; Thuburn and Craig 2002). The main evidence against significant effects has been thermal estimates of cloud-top height, but these are biased low even in individual satellite pixels (Sherwood et al. 2004). Low biases are significantly worse if radiances are averaged over larger time and space scales [e.g., in pentad outgoing longwave radiation (OLR) products], and tend to reflect only the outward spreading anvil clouds rather than the taller overshooting tops. Even a small percentage of higher-than-average cloud penetrations can compete with the much slower radiative and advective processes that dominate in the stratosphere. Various studies have indicated an important role for convection in determining temperature (Kuang and Bretherton 2004; Sherwood et al. 2003), water vapor (Read et al. 2004; Sherwood and Dessler 2001), and other tracer profiles (Dessler 2002) near the cold point. By simplifying the model physics as much as possible (i.e., excluding radiation and using warm rain Kessler microphysics) our investigation focused on the response of turbulent entrainment, large-scale ascent, and convective cooling to specific details of the numerical simulations such as convective available potential energy, subgrid model, domain size, resolution, and geometry.

Though the Brewer–Dobson circulation was first assumed to be upward throughout the deep Tropics, it was inferred first from Doppler radar (Gage et al. 1991) and then radiosonde data (Sherwood 2000) that a small downflow occurs in the upper part of the TTL above Indonesia. Wind reanalyses also show a downward mass flux in the western Pacific region (Simmons et al. 1999). Since sinking warms a stable layer, long-term energy balance dictates that some compensating heat sink must exist. Because horizontal energy transports are small, there must also be a mechanism by which this excess heat is removed. One possibility is cooling by convective overshoot. A parcel mixing model by Sherwood and Dessler (2001) of overshoots into the TTL was able to predict roughly the convective cooling required to drive the sinking. A similar circulation was driven by overshooting jets in laboratory experiments (Larson and Jönsson 1995). However, it has not yet been confirmed whether this connection truly exists in the tropopause region.

In this paper we describe a series of simulations using a cloud-resolving model to simulate deep convection in the Tropics. We will first describe the model and results from a typical simulation (control case) that indicates a role for convective overshooting and mixing. We then investigate the robustness of the convective effects (entrainment, plumes, heat transport by large-scale circulation and resolved eddies).

2. Cloud-resolving model

The simulations in this paper were computed using the Weather Research and Forecasting (WRF) model, which solves the fully compressible hydrodynamic (Navier–Stokes) equations (Wicker and Skamarock 2002). It uses a third-order-accurate Runge–Kutta scheme for the time integration, and second-to-sixth-order accurate spatial discretization is available for the advection terms. The model supports closed periodic or open lateral boundaries, and variable vertical grid spacing. The top boundary is a rigid lid and the bottom free slip. The available physics components in WRF include several microphysics packages, cumulus parameterization, longwave radiation, shortwave radiation, boundary layer turbulence (PBL), surface layer, land surface parameterization, and subgrid-scale diffusion. We tested WRF V1.3 (released March 2003) and WRF V2.0 (released in May 2004), with similar results. All results in this paper were computed using WRFV2.0.

3. Control case

a. Initial setup

We ran the model in the simplest possible situation: 2-D, no radiation, simple Kessler microphysics (Kessler 1969), no freezing of condensate, zero horizontal mean flow, and a horizontally uniform initial state specified from a June–August (JJA) mean Maritime Continent region sounding. The initial sounding included an 18 g kg^{-1} mixing ratio of water vapor below 1 km and was initially supersaturated from 0.74 to 2.2 km. This caused the immediate formation of a low cloud layer. Tests with subsaturated boundary layers reproduced the key results presented in the paper, although differing in some important respects that will be noted.

Zero horizontal flow reduces the chance of gravity wave breaking (Lane et al. 2003), which is something we preferred to avoid initially as it complicated our energy budget analysis. Lack of ice microphysics simplifies sensitivity studies, as ice processes are highly nonlinear. Radiation was neglected because it is of secondary importance in simulations that are so short (a few hours) compared to the radiative time (tens of days; Hartmann et al. 2001). We verified that this was a reasonable assumption by running two identical simulations up until the point at which convection first reached the TTL and then continuing one simulation with shortwave and longwave radiation switched on, and the other with it left off. The convective development over the next 2 h in the two cases was almost identical.

To enable us to study the interaction between convective-scale and large-scale motions, we used open boundaries in the across-line direction. With periodic walls, a realistic circulation cannot develop as any mass flow out a side wall will appear as an inflow at the other side of the computational box. We verified that the open boundaries could deal with horizontally propagating gravity waves by inserting a very small amplitude oscillating temperature source at the base center of the domain. By varying the frequency of the oscillation, the characteristic diagonal beams associated with the dispersion relation of internal gravity waves appeared clearly. When we computed the energy budget, we split the contributions to the temperature change into large-scale circulation and small-scale convective eddies. Provided the amplitude of the gravity waves was small at the side walls, then the balance was very good.

The uppermost 8 km contained an absorbing layer or sponge. In this layer, motions were damped by locally increasing the viscosity. To ensure that any wave reflection from the top lid did not affect our results, the control simulation was run with the top located at 24, 28, and 32 km. For the top at 28 and 32 km, the characteristics of convection in the TTL were almost the same, while the maximum convective flux was about 20% larger when the top was at 24 km.

To initiate convection near the center of the domain, a localized warming was applied gradually at the surface. The heating function at the ground was defined by adding a small perturbation p to the temperature T at the lowest level and $p/2$ to the temperature at the second lowest level, where p is

$$p = A_o \exp[-(x - 1/2)^2/b]tT. \tag{1}$$

By gradually creating a surface hot spot, we created instability in the most natural way and allowed the model to redistribute the surface energy through the boundary layer rather than imposing warm bubbles in the air itself. The horizontal distance x is scaled by the size of the domain L_x. When time t exceeded a certain value τ_c, then $p = 0$. A_o, b and τ_c were such that the maximum temperature perturbation was up to 8 K, depending on the desired convective available potential energy (CAPE).

A convection simulation with a particular CAPE and CAPE evolution could be generated by specifying a particular set of these three parameters. The control case was a 2D simulation with $L_x = 600$ km, $b = 0.1$, $\tau_c = 62.5$ min, with the heating source extended over the central 100 km. The grid was 1200×200 points with horizontal spacing of 500 m. The vertical spacing ranged from 570 m near the surface to 76 m at 18 km above the ground. As we are interested in resolving eddies in the TTL, we used a stretched vertical grid with the grid spacing small enough to resolve a range of convective eddies in the TTL and gravity waves in the upper layers. To achieve this we computed the wavelength of gravity waves (with a dispersion relation prescribed at the top) and made sure that waves horizontally and vertically resolved in the upper troposphere remained vertically resolved to at least 25 km (the top of the domain was at 28 km). The importance of this in obtaining realistic mixing was pointed out by Kuang and Bretherton (2004) and confirmed by our own tests. A detailed grid sensitivity study showed that results were far more sensitive to vertical than to horizontal resolution. We also tested with different vertical grid point distributions including uniform resolution up to 16 km, and found that provided the grid spacing was smaller than the wavelength of gravity waves (in the TTL and up to 25 km) and motions were resolved in the lowermost levels, then the properties of the simulations were similar. Horizontal grids of 250 m, 500 m, and 1 km produced very similar results. Details of the horizontal and vertical grid study are given later in section 4e. A plot of the initial temperature versus height is shown in Fig. 1 with the locations of the vertical levels marked by triangles.

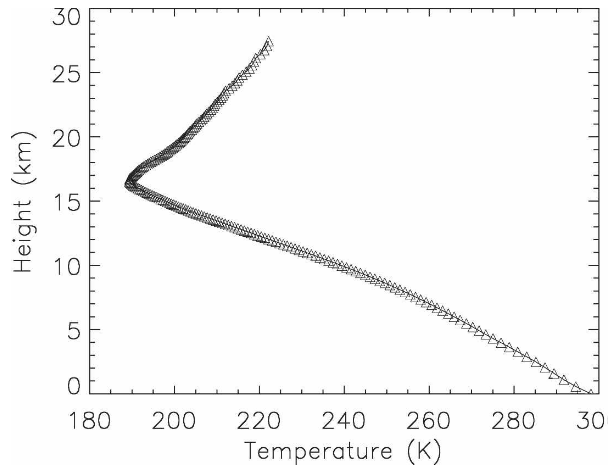

FIG. 1. Horizontally averaged temperature vs height at start of the control simulation. The triangles mark the locations of the 200 vertical levels. The vertical spacing ranges from 570 m near the surface to 76 m at 18 km above the ground.

b. Storm development

Figure 2 shows the time evolution of local CAPE and maximum vertical velocity w_{max} scaled by their maximum values, which are 3500 J kg^{-1} and 51 m s^{-1}, respectively. The "local" CAPE was computed by averaging the model state over the central 100 km of the domain, that is, directly above the heating source. The calculation was based on a pseudoadiabatic, nonentraining parcel from the lowest model level (located at 965 mb). Latent heat of freezing was excluded from the computation. The CAPE away from the local heating (in the initial sounding) was 1200 J kg^{-1}. The maximum vertical velocity of 51 m s^{-1} is near the upper range of observed peak updraft speeds in continental, tropical thunderstorms, but not unreasonable (Simpson et al. 1993).

The initial rise of the CAPE was the response to the heating source, which lasted for 62.5 min. Between 50 and about 60 min, the CAPE was approximately constant while w_{max} grew steadily. During this time, turbulent eddies are forming near the base and mixing boundary layer air with air aloft. More eddies form in the upper levels and produce a positive convective heat flux in the lower troposphere. These combine to form coherent plumes tens of kilometers across. The first four spikes in w_{max} show that these thermals formed about every 20 min during the main part of the convective life cycle.

At about 60 min, a large plume formed and w_{max} rose rapidly while the CAPE dropped to about a third of its maximum value. At this time the plumes had enough momentum to squash the lowermost stratospheric isentropes close enough together so that the maximum $\partial\theta/\partial z$ occurred in the TTL. This was the start time of our budget and mixing analyses of the run.

Figure 3 shows four snapshots of the cloud and temperature fields over the next hour. The growth of the cumulus convection is clearly evident, as is the spreading out of the anvil. We computed flow statistics between 72 and 131 min, during which time the amplitude of the gravity waves near the side walls remained small. As we have only confirmed the ability of the open boundary condition to handle small-amplitude gravity waves, we set the end time of the statistical integration to be before the gravity waves have a significant amplitude near the side walls. Figure 4 shows that precipitation-sized particles did not form until about 60 min. The amount of suspended precipitation grew until about 90 min then rained out so that the accumulated surface precipitation grew quickly. After about 300 min, the rate of precipitation remained constant at about 1/10 of the peak value.

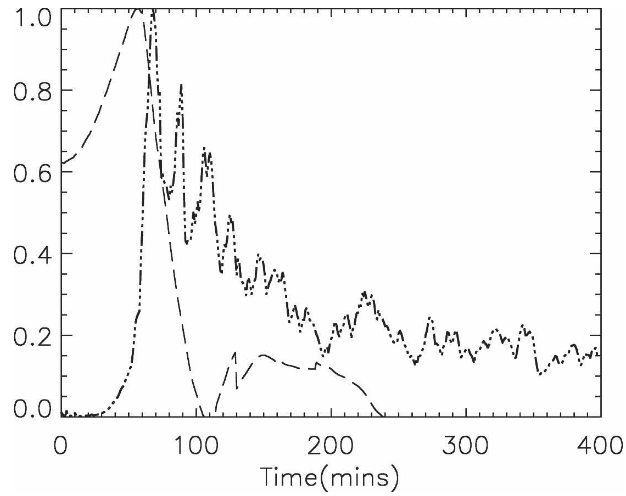

FIG. 2. Time evolution of local CAPE (dashed line) and maximum vertical velocity (triple-dot-dashed line) in the control simulation. Both are scaled by their maximum values, which are 3500 J kg^{-1} and 51 m s^{-1}, respectively.

By integrating the velocity field (postprocessing the WRF output) from $t = 0$ min to 132 min, we computed flow trajectories. Figure 5 shows the trajectories between 72 and 132 min of particles that at $t = 0$ min were at 17 km (blue) and 2 km (red). The horizontal black line marks the cold point in the input sounding located at 16.5 km. The blue trajectories that dip below the cold point represent stratospheric air that was being entrained by the overshooting cumulus turrets (red trajectories) and subsequently pulled 2–3 km below the initial cold point. The reported CAPE values are quite high because they are computed in the vicinity of the core of these updrafts (red tracks).

c. Turbulent heat flux

As there is very little latent heat at the heights characteristic of the TTL, nearly all dynamical temperature changes there are caused by sensible heat transport. This can occur in two ways:

1) large-scale circulation (net ascent or descent) producing reversible, adiabatic heat transport. We will denote the resulting temperature change by "C";
2) small-scale, intermittent, turbulent eddies producing an irreversible, diabatic flux (convective heat flux). We will denote the resulting temperature change by "T".

Note that this decomposition is not based simply on an arbitrary scale break, but on a more fundamental distinction between laminar and turbulent flow leading to reversible and irreversible changes of temperature, respectively. If the (open) model domain is imagined to

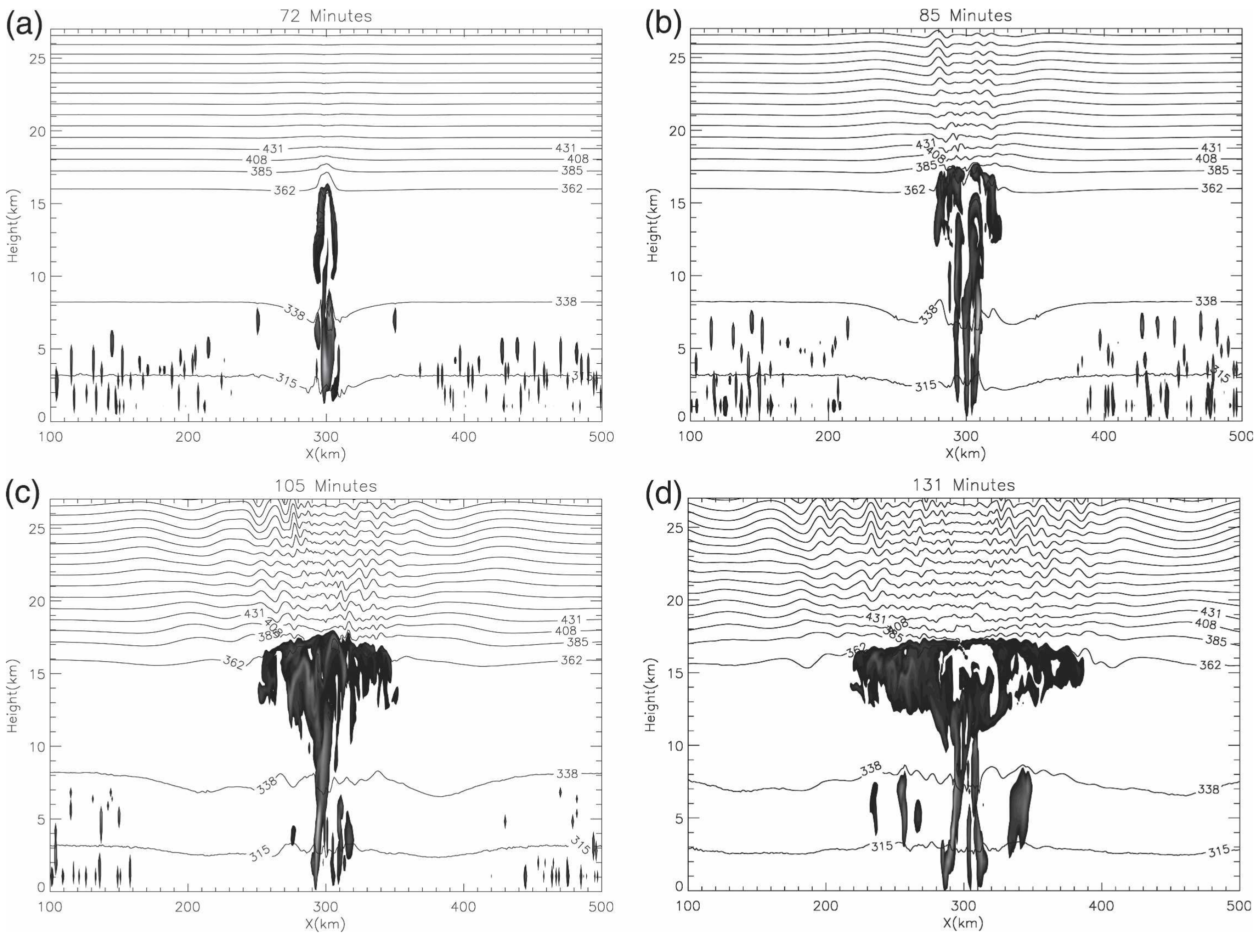

FIG. 3. Cloud water (dark shading) and potential temperature contours at four instants (a) 72, (b) 85, (c) 105, and (d) 131 min from the control simulation.

be embedded in a larger, closed domain, then only the irreversible part T would contribute to the thermal structure averaged over the larger domain, since the impact C of any net ascent or descent within the model domain would be compensated by opposite motions outside.

Turbulent mixing can either cool or warm a given layer. This is because convective heating/cooling is the net impact (horizontal average) of a series of turbulent eddies on a given horizontal layer. If there is on average more (less) heat leaving the layer than coming in, then the layer will cool (warm). This is a well-known feature of entrainment layers as seen in the case of the planetary boundary layer (e.g., Sullivan et al. 1998), the convection–radiation transition layer at the surface of the sun (Robinson et al. 2003), and laboratory experiments (Deardorff et al. 1980).

The convective heat flux is defined as

$$D = \overline{\rho w' \theta'}, \tag{2}$$

where ρ, w, and θ are the density, vertical velocity, and potential temperature, respectively. The fluctuating parts were computed as $w' = w - \overline{w}$ and $\theta' = \theta - \overline{\theta}$, so that the mean flow has been subtracted and the flux represents the net effect of turbulent eddies. The overbar represents a horizontal average, which in the 2D cases were taken over the central 300 km of a domain.

Figure 6 shows $D/D_{\max}$ as a function of height for the control simulation. The upper plot shows the instantaneous horizontal averages over the first hour of integration (at 10-min time intervals) and the lower plot the time average (with the averaging time indicated). The fluctuations (thin lines) were due to gravity waves. These canceled out if averaged over a few minutes. Averaging over 1 or 3 h produced almost the same magnitude for $D/D_{\max}$ but for the 3-h averaging, $D_{\max}$ was located about 1 km lower down. This is because convection was much weaker over the second and third hour of integration (see Fig. 2). As the averaging time was extended further, the ratio of $D_{\min}$ to $D_{\max}$ became

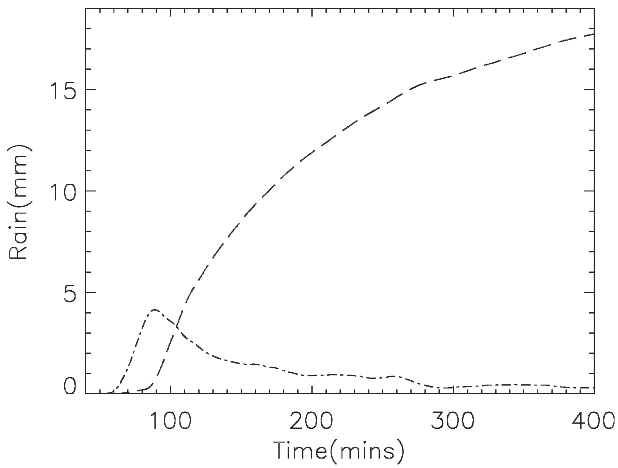

FIG. 4. Accumulated surface precipitation (dashed) and suspended raindrop volume (dot–dashed), each in millimeter-equivalent water depth in the control simulation.

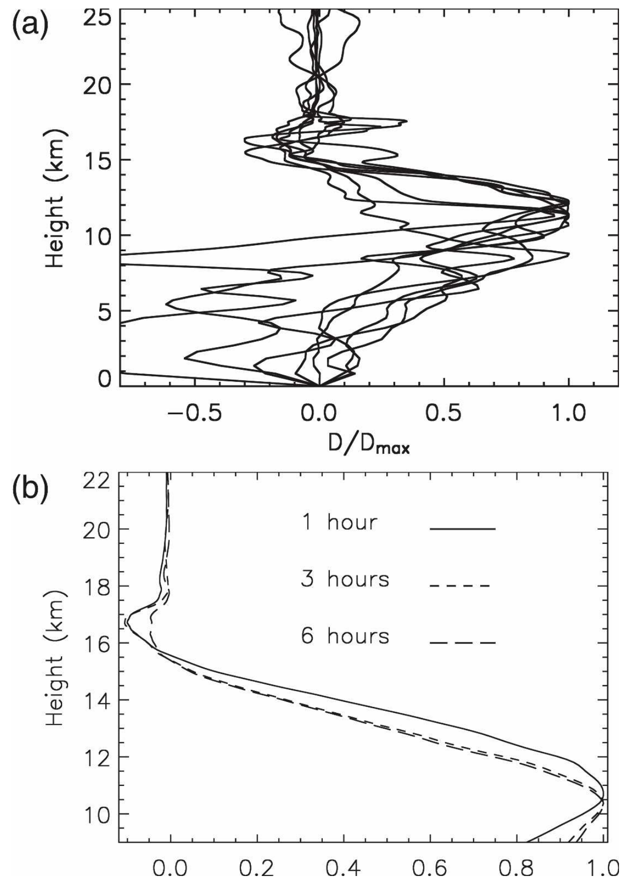

FIG. 6. The ratio of the turbulent heat flux (D) to its maximum value in the troposphere (D_{max}) for the control simulation. (a) The instantaneous D/D_{max} at 10-min intervals. (b) The 1-, 3-, and 6-h time average of D/D_{max}.

smaller and smaller. The time average represents an irreversible mixing process, which we found in all the simulations. The main region of negative convective heat flux lies between about 15.75 and 18 km, reaching a minimum at16.7 km, just above the cold point.

Looking at the corresponding trajectory plots (Fig. 5) one can see that some fluid overshot the cold point and brought higher θ air downward. This entrainment of laminar stratospheric air provided a negative contribution to D so that between about 17 and 18 km $\partial D/\partial z$ was positive and the layer was convectively cooled. In other words, the overshoot has $w' < 0$ and $\theta' > 0$, which reduces $\overline{\rho w'\theta'}$ and increases $\partial(\overline{\rho w'\theta'})/\partial z$. The layer loses heat and cools.

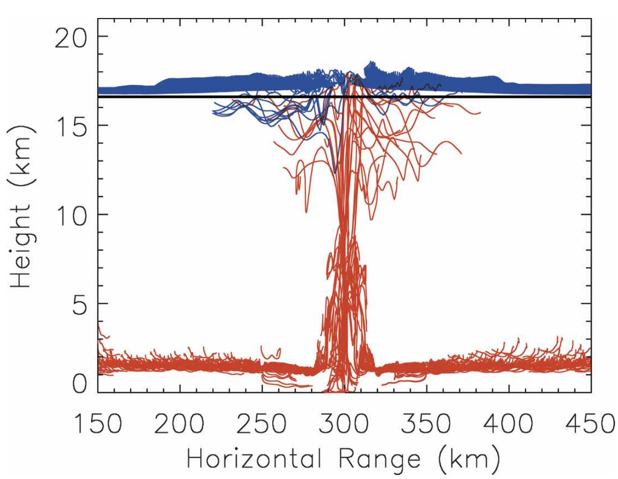

FIG. 5. Particle trajectories between 72 and 132 min for the control simulation. The particles were originally at 2 (red) and 17 km (blue), and the black horizontal line marks the cold point in the initial sounding.

This cooling peaked roughly 1 km above the cold point in the background profile. This was found by Kuang and Bretherton (2004) to be crucial in determining the cold point temperature itself over longer time scales. The entrainment of lower stratospheric air into the upper troposphere is potentially relevant to distributions of trace species created or destroyed in the stratosphere, such as ozone.

d. Energy budget

The WRF model uses hydrostatic pressure π as the vertical coordinate. The contribution C to the energy budget from large-scale circulation is equal to the product of the circulation velocity and the mean temperature gradient (both are horizontally averaged). The circulation velocity was computed by vertically integrating the horizontally averaged mass divergence. In the coordinate system used by WRFV2.0 the circulation velocity (similar to a pressure velocity) $\Omega^*(\eta, t)$ is

$$\Omega^*(\eta, t) = -\int_{\eta=0}^{\eta} \left[\frac{\partial \overline{\mu}}{\partial t} + \frac{(U_r - U_l)}{L_x} \right] d\eta, \tag{3}$$

where $\mu = \pi_s - \pi_t$, $\eta = [(\pi - \pi_t)/\mu]$. Here $U = \mu u$, and $\Omega = \mu\, d\eta/dt$ represent the column mass, vertical mass coordinate, horizontal velocity (in the mass coordinate system), and the hydrostatic pressure velocity, respectively. The subscripts s, t, r, and l, denote the surface, top, right boundary, and left boundary of the domain, respectively, and L_x is the total domain width. The overbar denotes averaging in the horizontal plane.

In the WRF coordinate system the convective heat (enthalpy) flux is written as $\overline{\Omega'\theta'} = \overline{(\Omega - \overline{\Omega})\ (\theta - \overline{\theta})}$, where the overbar again denotes a horizontal average. This represents the diabatic heat flux D [Eq. (2)].

In terms of the above two contributions, the horizontal mean rate of change of the potential temperature can be written as

$$\frac{\partial \overline{\Theta}}{\partial t} \approx -\Omega^* \frac{\partial \overline{\theta}}{\partial \eta} - \frac{\partial}{\partial \eta} \overline{\Omega'\theta'}, \tag{4}$$

where $\Theta = \mu\theta$. The first and second terms of the right-hand side represent the effect of C and T.

Figure 7 shows the contributions of C (triple-dot dash) and T (long dashes) to the temperature change (solid line) observed over 1 h. From 15–25 km (where the grid is fine enough to resolve gravity waves and convective eddies), the energy budget was satisfied to within a few percent, so our decomposition reliably captures the essence of the heat budget. This also suggests the heat flux by the unresolved eddies (subgrid-scale conduction/diffusion) was very small in this region. This was confirmed by comparing the parameterized TKE with the resolved TKE. Between 10 and 25 km, the peak in the resolved TKE was always at least 30 times that of the subgrid-scale TKE. This was true for all the simulations.

e. Height of the top of the entrainment layer

We used three methods to define a single entrainment (mixed) layer top altitude for a simulated event.

1) At each horizontal grid location x and time t (with 1-min time intervals), compute the height $z_1(x, t)$ where the static stability $\partial\theta/\partial z$ reaches its maximum. At each t, compute the horizontal mean of all $z_1(x, t)$ values that are between 15 and 20 km. Then average those z_1 values over the hour of the convective event. This choice was motivated by the definition of PBL height used by Sullivan et al. (1998).
2) Average in the same way the cloud-top height $z_2(x, t)$ defined as the level above which the integrated cloud water content is 0.02 kg m^{-2} or approximately the level of unit optical depth. Again, the horizontal average was taken only over x at which z_2 lies above 15 km and then average those z_2 values over the hour of the convective event. For the control case the peak cloud-top height can exceed 18 km.
3) For each horizontal grid point, compute the top of the TKE surface. This is done by averaging over all the points for which the nonzero TKE at grid point k is less than that at $k + 1$, the value of TKE at grid point $k + 2$ is zero and the grid point itself is between 15 and 20 km above the ground. This was then averaged horizontally then over time. This height is denoted z_3.

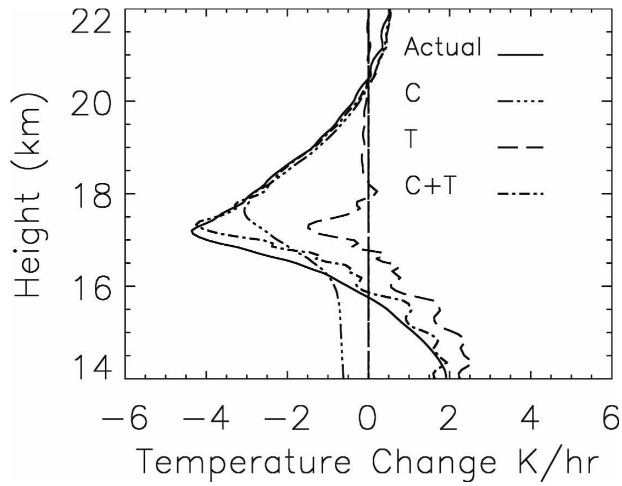

FIG. 7. Horizontally averaged temperature change over 1 h (solid line) in the control simulation. Contributions to the temperature change from large-scale circulation C and small-scale eddies T are denoted by triple-dot dashes and long dashes, respectively. The combined effect of small and large scales (T + C) is denoted by the dot–dashed line.

In all of the simulations we found that z_2 and z_3 were almost the same (typically $|z_2 - z_3| \leq 0.1$ km, while z_1 was about 1 km higher up. Consequently, from now on we will only give values of z_1 and z_2, with z_2 representing both cloud-top height and TKE-top height.

4. Sensitivity study

a. Local CAPE

Heating the base over a longer time increased the local CAPE for a particular convective event. Figure 8 shows the mean temperature change (averaged over the central 100 km) between the start of the simulation and the time of maximum CAPE (just before the start of the convective episode). As deep convection had not started yet, most of the temperature change was confined to the region of local heating (near the ground).

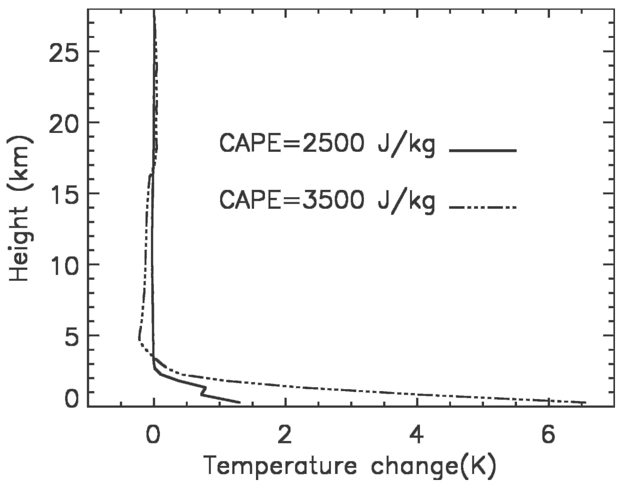

FIG. 8. Change in background temperature between the start of the simulation and the time of maximum CAPE.

The simulations in Table 1 are identical to the control case except for the amount of time τ_c the localized heating is applied and, therefore, the maximum CAPE that developed prior to convective onset. From left to right, the columns in the table are the maximum local CAPE (averaged over the central 100 km), the time of applied heating (τ_c), the magnitude and location of the maximum temperature drop from the large-scale circulation (δT_{LS}) over the convective episode (1 h), the magnitude and location of the maximum temperature drop due to the turbulent heat flux (δT_{SS}) over the convective episode, the ratio of the minimum turbulent heat flux to its maximum tropospheric value averaged over 1 h (D_{min}/D_{max}) with vertical location in kilometers in brackets, the size and location of the mean maximum turbulent heat flux (D_{max}), and the two measures of the entrainment height z_1 and z_2. The next two columns are the maximum vertical velocity (w_{max}) with vertical location in brackets and the total accumulated precipitation (P) over the convective episode. All the other tables in this paper contain similar quantities. Unless otherwise specified, the heat source always extended over the central 100 km and the horizontal averaging was taken over the central 300 km. The tabulated values of D_{min}/D_{max}, D_{max}, z_1, and z_2 are all 1-h averages.

Not surprisingly, putting in more heat (increasing τ_c) produced stronger convection. As local CAPE was increased from 1900 to 3500 J kg^{-1}, the upward flux D_{max} in the upper troposphere increased by about a factor of 3, and other measures of convective intensity (P, w, convective heights) all increased. Importantly, the entrainment flux ratio D_{min}/D_{max} remained about -0.1 for every simulation. In other words, a downward heat flux near the tropopause always occurred that was about 10% of the peak upward flux in the middle-to-upper troposphere. If the averaging time (in the control case) was increased to 3 h or to 6 h, then the entrainment flux ratio was -0.11 (at 16.7 km) and -0.05 (at 16.3 km), respectively (see lower panel of Fig. 6). The bulk contribution to the convective flux came from the main part of the convective life cycle, which was the first 60–100 min after the onset of convection. This result reinforces the analogy between the TTL and other entrainment layers, where similar ratios are observed between the upward heat flux near the lower boundary and that in the entrainment zone. Furthermore, our 1/10 ratio is within the range previously encountered (Deardorff et al. 1980; Fedorovich and Conzemius 2004; Moeng et al. 2004).

To quantify the entrainment associated with this cooling process in a way more relevant to tracer transport, we computed the probability that a particle starting in the TTL has a potential temperature below 370 K at the end of the convective event. Figure 9 is the corresponding plot (with probability on the x axis) for the simulations with CAPEs of 2500 and 3500 J kg^{-1} versus initial height (left vertical axis) and initial potential temperature (right vertical axis). Figure 10 shows the corresponding turbulent fluxes.

TABLE 1. Convection characteristics for a series of 2D simulations. The local maximum CAPE was adjusted by varying the time (τ) over which heat was applied to the base (the background CAPE was 1200 J kg^{-1}). All other conditions were the same as in the control simulation denoted by *.

CAPE, (max; J kg^{-1})	τ_c (min)	δT_{LS} (K h^{-1})	δT_{SS} (K h^{-1})	D_{min}/D_{max}	D_{max} (kg m^{-2} s^{-1} K)	z_1 (km)	z_2 km	w_{max} (m s^{-1})	P (mm h^{-1})
1900	20	−0.75 (16.8)	−0.2 (15.7)	−0.11 (15.2)	0.29 (9.8)	17.9	15.9	24 (11)	4.1
2500	40	−1.4 (17.0)	−0.3 (16.7)	−0.1 (15.9)	0.44 (11)	17.5	16.2	32 (13)	4.7
2800	45	−1.8 (17.1)	−0.36 (17)	−0.11 (15.9)	0.59 (10.4)	17.4	16.4	48 (13)	5.4
2970	47.5	−2.2 (17.3)	−0.75 (17)	−0.09 (16.4)	0.62 (10.6)	17.4	16.6	35 (11)	5.5
3150	50	−2.3 (17.3)	−1.1 (17.2)	−0.1 (16.5)	0.62 (10.7)	17.5	16.6	44 (14)	5.7
3450	55	−2.6 (17.4)	−1.4 (17.1)	−0.11 (16.7)	0.93 (10.8)	17.5	16.8	46 (12)	6.4
3500*	62.5	−3.1 (17.6)	−1.5 (17.3)	−0.1 (16.7)	0.93 (10.8)	17.7	17.1	51 (10)	6.7
3520	70	−3.8 (17.7)	−2.0 (17.7)	−0.1 (16.9)	1.2 (10.9)	17.8	17.2	55 (12)	7.4

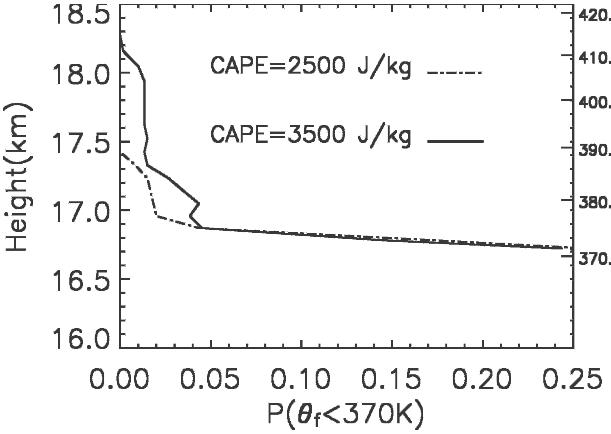

FIG. 9. Probability of a particle having a potential temperature θ_f below 370 K at the finish of its convective episode vs initial height or initial potential temperature θ_i.

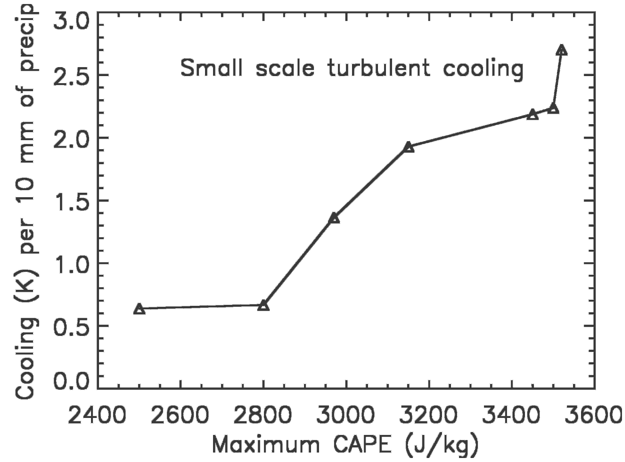

FIG. 11. Maximum temperature change in the TTL due to turbulent eddy heat flux per 10 mm of surface precipitation.

The peak temperature drop δT_{SS} in the TTL associated with turbulence was even more sensitive to CAPE than D, increasing by almost a factor of 10 over the same CAPE range. This strange result is explained by noting that δT_{SS} is determined by the vertical derivative of D. As CAPE increased and convection penetrated farther into the stable layers of the TTL (viz., increases in z_2), the location of D_{min} moved up much closer to the cold point in the sounding. The vertical derivative of D, hence δT_{SS}, increased sharply as the entrainment zone became more compressed. This increase was much faster than that of precipitation (Fig. 11). It is interesting that the increased stability encountered by the stronger convection has compensating effects on the turbulence (which is weaker) and on the temperature fluctuations (larger) so as to keep the entrainment flux ratio constant.

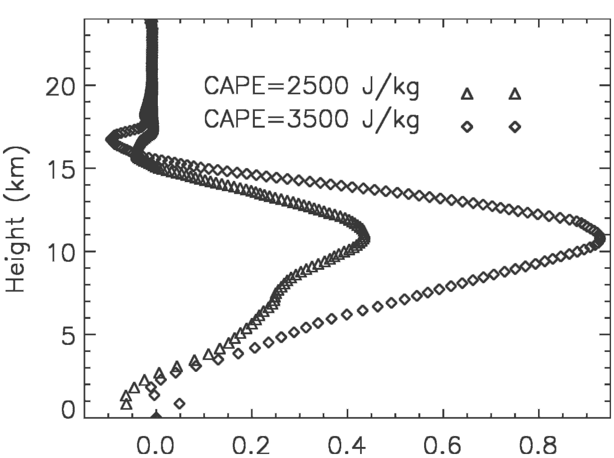

FIG. 10. One-hour average of the turbulent convective flux $D = \overline{\rho w'\theta'}$ (kg m^{-2} s^{-1} K) for the two simulations in Fig. 9.

For a CAPE of 3500 J kg^{-1} overshoot pulled fluid from as high as 18.25 km down below the cold point. Only about 1% of the air from between 17.5 and 18.25 km is brought down below the cold point, but even such a small amount of this high θ air produced a convective cooling almost 5 times greater than the lower CAPE case. Sherwood and Dessler (2001) showed that such entrainment of stratospheric fluid into the troposphere is directly connected to diabatic cooling below the level of highest entrainment.

b. *Effect of turbulence model on the entrainment flux ratio*

Two of the subgrid models available in WRFV2.0 are the turbulent kinetic energy model (e.g., Klemp and Wilhelmson 1978) and the Smagorinsky–Lilly (S–L) model (Lilly 1962). In both closures the small-scale energy sink is viscous dissipation. With one exception, the simulations presented in this paper all use the TKE model.

The aim of a subgrid model is to close the system of equations by parameterizing the unresolved Reynolds stresses in terms of resolved quantities. The corresponding term in the momentum equation is

$$-\frac{\partial}{\partial x_j}(\overline{u_i' u_j'}), \tag{5}$$

where $u_i' u_j'$ is the unresolved Reynolds stress. The TKE models uses

$$\overline{u_i' u_j'} = -K_m\left(\frac{\partial u_i}{\partial x_j} + \frac{\partial u_j}{\partial x_i}\right) + \frac{2}{3}\delta_{ij}K, \tag{6}$$

TABLE 2. Convection characteristics for a series of 2D simulations in which a parameter in the turbulence model was adjusted. All other conditions were the same as in the control simulation denoted by an asterisk (*).

SGS model	δT_{LS} (K h^{-1})	δT_{SS} (K h^{-1})	D_{min}/D_{max}	D_{max} (kg m^{-2} s^{-1} K)	z_1 (km)	z_2 (km)	w_{max} (m s^{-1})	P (mm h^{-1})
$c_k = 0.25$*	−3.1 (17.6)	−1.5 (17.3)	−0.1 (16.7)	−0.93 (10.8)	17.7	17.1	51 (10.4)	6.7
$c_k = 0.5$	−2.9 (17.5)	−0.9 (17.3)	−0.09 (16.9)	−0.97 (10.9)	17.8	17.1	49 (13)	7.2
$c_k = 1.0$	−2.4 (17.9)	−1.6 (17.4)	−0.14 (17)	−0.94 (11.3)	17.8	17.2	46 (10)	7.0
S–L, $c_s = 0.25$	−2.3 (17.2)	−1.1 (17.3)	−0.13 (16.9)	−0.84 (11.0)	17.8	17.0	45 (13.6)	7.55

where

$$K_m = c_k K^{1/2} \Delta \tag{7}$$

and

$$K = \frac{1}{2}(u_i')^2. \tag{8}$$

The length-scale Δ is determined by local grid spacing and the stratification. The equation for the turbulent kinetic energy K is solved by parameterizing transport, buoyancy, and dissipation in terms of the resolved flow quantities. The parameter c_k is set to 0.25, a value based on 3D, homogeneous, isotropic turbulence.

Table 2 indicates that as c_k was increased from 0.25 to 1.0, the cooling by mean ascent δT_{LS} and the maximum vertical velocity both decreased. This is because increasing the eddy viscosity K_m slowed down the mean/overall flow.

The other tabulated quantities do not exhibit such monotonic behavior because they depend on the entrainment dynamics of the TTL. While a higher viscosity slows down the overall flow, it also causes more air to be entrained from the stratosphere into the underlying troposphere by overshoot. The entrainment flux ratio D_{min}/D_{max} (column 4) was 50% higher for $c_k = 1$ compared to the lower c_k values, while the tropospheric flux D_{max} was similar for each c_k.

Increasing c_k slowed down the mean flow but also increased the entrainment flux ratio. The two effects seem to almost cancel each other out so that the convective cooling, convective flux, and precipitation were almost the same for $c_k = 0.25$ and $c_k = 1$.

One other subgrid model available is the Smagorinsky–Lilly model, in which

$$\overline{u_i'u_j'} = -K_m\left(\frac{\partial u_i}{\partial x_j} + \frac{\partial u_j}{\partial x_i} - \frac{2}{3}\delta_{ij}\frac{\partial u_k}{\partial x_k}\right) \tag{9}$$

$$K_m = (c_s\Delta)^2|S|\sqrt{1 - R_i/P_r}\colon (1 - R_i/P_r) > 0 \tag{10}$$

$$S^2 = \frac{1}{2}\left(\frac{\partial u_i}{\partial x_j} + \frac{\partial u_j}{\partial x_i}\right)^2. \tag{11}$$

The parameters c_s and Prandtl number P_r are set to 0.25 and 1/3; $R_i = N^2/S^2$ is the local Richardson number, where S and N are the viscous dissipation and Brunt–Väisälä (B–V) frequency, respectively.

One disadvantage of the S–L model is that the viscosity switches from a grid/flow-dependent value to a constant value when $(1 - R_i/P_r) < 0$. This sometimes caused the simulation to crash. The simulation seemed to improve if K_m was averaged horizontally about three grid points:

$$K_m(i, j) = [K_m(i-1, j) + 2K_m(i, j) + K_m(i+1, j)]/4 \tag{12}$$

and the same in the other horizontal direction for 3D flows. The last row of Table 2 contains the results with the S–L model. The entrainment flux ratio of the S–L model is similar to the most viscous TKE model.

c. Domain width

If the open boundaries are operating correctly, then they should not interfere with the development of the cloud. The storm should develop as if there were no boundaries at all. To test the effectiveness of the open boundaries we compared simulations with 300-, 600-, and 1200-km horizontal extent. The convection characteristics are given in Table 3. If we compare the first three rows of Table 3, we can see that the boundaries had little effect on the convective part of the energy budget. This is to be expected as the convective overturning was mostly confined to the center of the domain. The temperature change due to large-scale circulation increased by 300% if the domain was doubled, but only by 33% if it was doubled again. This suggests that the open boundaries are only partially effective in permitting large-scale ascent, but that a 600-km domain appears sufficient to allow natural development over the short time scale of interest here.

d. Microphysics

The values in row 4 of Table 3 are from a simulation that uses the WRF2.0 microphysics option 3 based on

TABLE 3. Convection characteristics for a series of 2D simulations in which the horizontal domain size L_x was adjusted (first three rows) or ice microphysics was included (last row). All other conditions were the same as in the control simulation denoted by an asterisk (*). In the ice case, the precipitation developed differently and reached maturity about an hour after the first convective episode. The precipitation over the convective episode was only 2.2 mm. The value in parentheses is the precipitation when the accumulated surface precipitation equaled twice the suspended rain.

L_x (km)	δT_{LS} (K h^{-1})	δT_{SS} (K h^{-1})	D_{min}/D_{max}	D_{max} (kg m^{-2} s^{-1} K)	z_1 (km)	z_2 (km)	w_{max} (m s^{-1})	P (mm h^{-1})
300	−1.3 (17.5)	−1.5 (17.2)	−0.1 (16.5)	0.97 (11.1)	17.7	17.0	51 (15)	6.91
600*	−3.1 (17.6)	−1.5 (17.3)	−0.1 (16.7)	0.93 (10.8)	17.7	17.1	51 (10.4)	6.7
1200	−3.4 (17.6)	−1.3 (17.1)	−0.1 (16.7)	0.86 (10.9)	17.7	16.9	50 (12)	7.0
600 (Ice)	−2.4 (17.2)	−2 (17.8)	−0.15 (17.3)	1.1 (11.7)	18.1	17.3	62 (14)	2.2 (11.7)

Hong et al. (1998). This includes ice microphysics as opposed to only the Kessler warm rain microphysics used in all the other simulations. By comparing rows 2 and 4, we can see that including ice reduced the cooling by large-scale ascent, but increased the amount of convective cooling per hour in the TTL. The inclusion of ice microphysics increased the entrainment flux ratio by 50% and produced overall stronger convection (D_{max} increased by 20% and the entrainment layer was about 1 km higher up). These combined to cool the TTL by 2 K h^{-1} compared to 1.5 K h^{-1} in the control case. Above the melting height, ice can form and give an additional push to the buoyancy (from the latent heat of fusion). The additional acceleration enabled plumes to reach to greater heights and thus entrain higher θ air into the upper troposphere. This was probably responsible for the increase of the convective flux and cooling in the TTL.

e. Grid resolution

To assess the role of vertical resolution we compared three simulations that were identical other than having 100, 200 (control case), and 400 stretched vertical grid levels. The first vertical grid level above the ground was at 1100, 570 (control case), and 285 m, for 100, 200, and 400 vertical grid levels, respectively. Figure 12 shows the evolution of the maximum vertical velocity on each grid. Clearly, vertical resolution near the ground strongly influenced both the triggering and the subsequent development of convection (the evolution of the maximum CAPE, though not shown, was about the same in each case). For 100 vertical levels there was about a 20-min delay before the maximum velocity grew appreciably, but once things start moving, the convective motions were much faster. Because the first vertical grid level was more than 1 km above the ground, fluid parcels needed more buoyancy to overshoot the level of free convection, but once they had, they traveled much faster. For N_z equal to 200 and 400, the evolution of the vertical velocity was more similar.

Convection characteristics for the three vertical resolutions are given in the first three rows of Table 4. Both mean (δT_{LS} and w_{max}) and turbulent (δT_{SS}, D_{min}/D_{max}, and D_{max}) quantities were much larger on the $N_z = 100$ grid than on either of the finer grids.

Horizontal resolution was far less important. The fourth and sixth rows of Table 4 are from simulations that were identical to the control case except for the horizontal resolution. The tabulated quantities were not affected much by changes in horizontal grid spacing.

5. Comparing 2D and 3D convection

One issue is whether a third dimension is really necessary in the domain. Even though 2D turbulence has fundamental differences to 3D turbulence, it has been shown by Moeng et al. (2004) that under certain conditions (with particular values of the constants in the turbulence subgrid models) the 2D convective flux in the planetary boundary layer can quite closely resemble the 3D counterpart. They found that certain properties

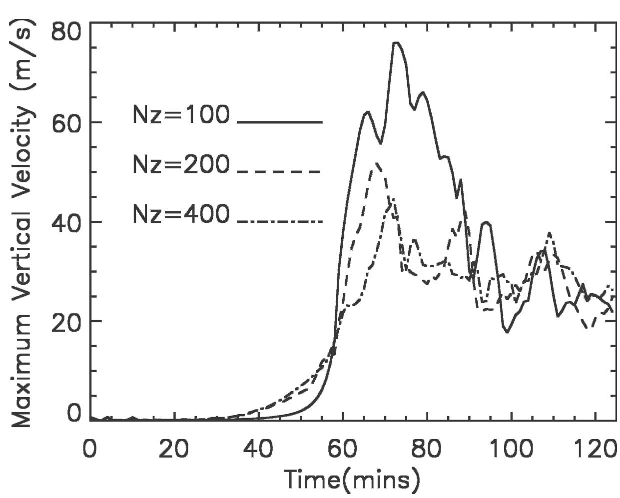

FIG. 12. Maximum vertical velocity for different vertical grids.

TABLE 4. Convection characteristics for a series of 2D simulations for different numbers of vertical levels (N_z) or horizontal grid resolution (Δx). All other conditions were the same as in the control simulation denoted by an asterisk (*).

Grid spacing	δT_{LS} (K h^{-1})	δT_{SS} (K h^{-1})	D_{min}/D_{max}	D_{max} (kg m^{-2} s^{-1} K)	z_1 (km)	z_2 (km)	w_{max} (m s^{-1})	P (mm h^{-1})
N_z = 100	−3.5 (17.2)	−4.6 (18.4)	−0.2 (17.7)	1.9 (12)	18.6	17.8	76 (13)	7.1
N_z = 200*	−3.1 (17.6)	−1.5 (17.3)	−0.1 (16.7)	0.93 (10.8)	17.7	17.1	51 (10.4)	6.7
N_z = 400	−2.8 (17.3)	−1.3 (17.0)	−0.1 (16.5)	0.84 (10.6)	17.5	16.8	45 (10.3)	6.5
Δx = 250 m	−2.7 (17.6)	−1.3 (17.3)	−0.1 (16.7)	0.93 (10.8)	17.8	17.1	48 (14)	6.8
Δx = 500* m	−3.1 (17.6)	−1.5 (17.3)	−0.1 (16.7)	0.93 (10.7)	17.7	17.1	51 (10.4)	6.7
Δx = 1000 m	−2.7 (17.5)	−1.3 (17.3)	−0.09 (16.7)	1.0 (10.8)	17.8	17.0	39 (12.5)	6.7

such as the mean thermal structure were reasonably robust to 2D–3D changes. This was also found in a cloud-resolving model by Grabowski et al. (1998), turbulence simulations of the analogous capping region at the surface of the sun (Asplund et al. 2000) and for 2D and 3D simulations of compressible convection, which included entrainment layers and stably stratified layers at the same time (Muthsam et al. 1995). Reynolds stresses did, however, show noticeable differences in 2D and 3D simulations.

To get a 3D simulation that can be reliably compared to its 2D counterpart we need to have open boundaries in both x and y directions and use the same vertical grid as the control case. The surface heating was a 3D Gaussian equivalent to the 2D heating source. The alternative would be to have a ridge-shaped source. The problem with a ridge is that the convection will tend to develop into rolls with axes oriented in the y direction, so a comparison to 2D convection will be biased by the shape of the heat source. A 3D Gaussian or hill is essential to avoid any bias of forming "2D like" coherent structures. This also meant we required the same resolution in both the x and y directions. For a 600 km by 600 km horizontal domain with 500-m resolution this was beyond our available computational power.

As a compromise we chose to run a simulation with a 75 km × 75 km horizontal cross section using 500-m uniform grid spacing and the same vertical resolution as in the control case. This also enabled us to make a direct comparison of our 3D simulation with that of Kuang and Bretherton (2004), which was run on a 64 km by 64 km horizontal domain. Our simulation had 150 × 150 × 200 grid points. Running on four nodes with four processors took about 10 h of hard wall clock time on a National Center for Atmospheric Research (NCAR) supercomputer.

The heating was applied over the central 13 km of the domain so that we could analyze the convection properly with the open boundaries. For this 3D case the convection developed very quickly, with similar convective structures in the x–z and y–z planes. As the convection kicked off after about 20 min the maximum CAPE was about 1900 J kg^{-1}. This was low compared to the previous simulations.

As the large-scale circulation depends sensitively on the horizontal size of the box (section 4c) we could only reliably examine the small-scale part of the energy budget in the 3D simulation. The maximum convective cooling was 0.2 K h^{-1} (at 16 km), the entrainment flux ratio was −0.11 (at 14.9 km) and the precipitation 2.2 mm h^{-1}. The equivalent 2D simulation is the first row of Table 1. The convection characteristics are very similar.

Figure 13 shows the convective flux for the 3D simulation and the equivalent 2D simulation. The maximum convective flux is about 50% greater in the 3D simulation and occurred at about 8 km, compared to 10 km in the 2D case. However, the curves have about the same slope at 16 km so the maximum convective cooling was similar. The residual flux near the top in the 2D simulation was also found in a simulation of the planetary boundary layer by Moeng et al. (2004). They found that it could be removed by adjusting the diffusion param-

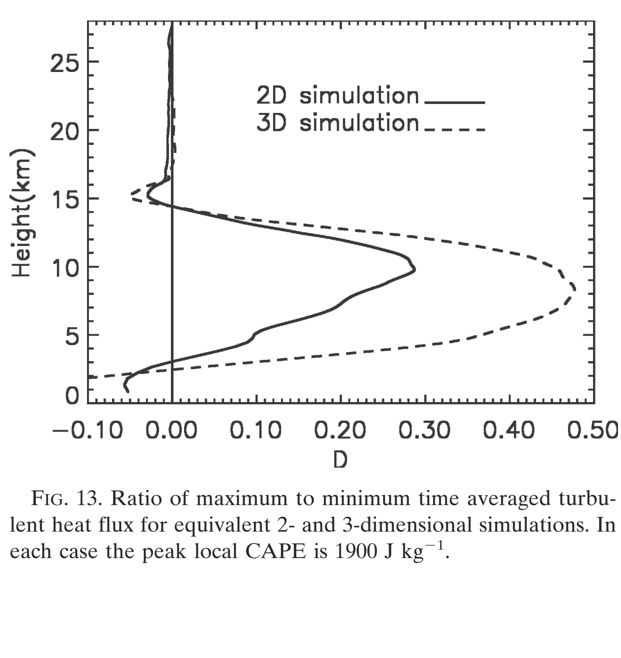

FIG. 13. Ratio of maximum to minimum time averaged turbulent heat flux for equivalent 2- and 3-dimensional simulations. In each case the peak local CAPE is 1900 J kg^{-1}.

eter c_k (section 4b), which modifies the resolved-scale flow.

Comparison with Kuang and Bretherton simulation

The main difference between the present study and that of Kuang and Bretherton (2004, hereafter KB) is that all of the integrations described in this paper are transient runs with an observed initial condition that have not reached thermal equilibrium, while the simulation by KB was of a radiative convective equilibrium state of a 64 km × 64 km × 40 km domain. In their case, they did not need an artificial heating source at the base and the CAPE was determined from the internal dynamics and thermodynamics of the model. Most of our simulations are 2D and we excluded radiation from the model focusing primarily on the turbulence characteristics of relatively short convective episodes (about an hour). Other differences are that we used open boundaries in the across-line direction, a much larger horizontal domain (in the 2D simulations), finer horizontal grid spacing (essential to study entrainment), and the TKE subgrid-scale turbulence model. Because we use open boundaries and KB use periodic boundaries we cannot compare the large-scale/mean ascent, but we can compare the details of the turbulent entrainment or convective cooling.

Kuang and Bretherton (2004) found a maximum convective cooling of 0.3 K day^{-1} (Fig. 3 in KB) at about 16 km, a mean precipitation of 3.5 mm day^{-1} (Z. Kuang 2005, personal communication) and a maximum vertical velocity of about 20 m s^{-1}. The peak CAPE was about 2800 J kg^{-1}.

Though most our simulations are for higher CAPE, the lowest ones compare quite favorably to the results in KB. For a CAPE of 2800 J kg^{-1} we found a maximum convective cooling of 0.36 h^{-1} at 17 km, a mean precipitation of 5.4 mm h^{-1} and a maximum velocity of 48 m s^{-1}. While in our 3D simulation, for a CAPE of 1900 kg^{-1}, we found a maximum convective cooling of 0.2 K h^{-1} at 16 km, a mean precipitation of 2.2 mm h^{-1} and a maximum velocity of 32 m s^{-1}. Assuming that convective overshooting only lasts for 1–2 h (over a day) then the convective cooling rates are approximately the same.

Note Küpper et al. (2004) ran a 3D radiative–convective equilibrium model under similar conditions to KB but with an imposed mean ascent to mimic the rising arm of the Brewer–Dobson circulation. In their case, overshoot was unable to penetrate above the cold point. They stated that their equilibrium model had relatively small CAPE. It is not clear whether the imposed ascent or other model details were responsible for the apparent difference in convective cooling of the tropopause between those studies. Since we find cooling similar to KB based on an observed sounding that implicitly includes the effect of any large-scale circulations actually present in nature, our results suggest that KB's tropopause cooling was not an artifact caused by the lack of these circulations.

6. Discussion

Through a comprehensive set of simulations we have found that air overshooting its level of neutral buoyancy consistently produces diabatic cooling near the tropopause, as implied by recent observational and model studies. This qualitative behavior was resistant to changes in grid resolution, domain size, microphysics, turbulence scheme, and model dimension. The cooling can be divided into two parts: an adiabatic cooling by large-scale ascent (due to heating farther down in the troposphere) and a small-scale irreversible mixing. The former was hard to interpret, and the amount was sensitive to model domain size and other design factors. It is likely due to the net effect of gravity waves leaving the domain; further study would be necessary to understand this behavior better. The small-scale mixing, however, was more robust, and was the main focus of the study.

The irreversible diabatic cooling in the TTL is associated with a reversal in the buoyancy flux analogous to that in other entraining layers, and occurs where the turbulent heat flux D is downward and is decaying to zero. The effect is caused by the forced mixing of low θ air in convective overshoots up to high levels, and the entrainment of high θ air from as high as 18.25 km above the ground, down to as far as a few kilometers below the cold point. This cooling was quantitatively robust, typically peaking a few hundred meters above the cold point in the profile. The large θ gradients that occur because of adiabatic lifting would appear to be important in enhancing the ability of penetrating turrets to mix air through potential temperature surfaces. The cooling peaked at an altitude higher than the mean cloud-top and TKE surfaces, but below the altitude at which potential temperature gradients attained their maximum during the convective event.

Our results compare well with those of the observational study of Sherwood et al. (2003) and the radiative–equilibrium simulations of KB. Unlike previous model studies, we simulated convective transients in an observed initial profile. This implicitly includes any effects of large-scale upwelling, and also allows us to examine via sensitivity studies the importance of quantities such as CAPE that exhibit significant geographical variations on earth. The diabatic cooling did not appear to reach sufficient altitudes to match the profile of apparent cooling noted by Sherwood (1999), remaining significant only up to 1–2 km above the cold point, but is probably a part of the explanation for the cooling and/or cold tropopause temperatures observed over regions of deep convection.

Entrainment of about 1% of the air above 18 km was sufficient to produce a cooling of more than 1 K h^{-1}. Given the long residence time of air above the cold point, even such a small entrainment rate will likely also prove consequential for the transport and ambient distribution of trace gases such as water vapor and ozone, and probably helps to explain the gradual increase of ozone typically observed below the tropical tropopause.

Increasing the CAPE caused the convection to be more energetic in the troposphere (higher $D_{\max}$) and to penetrate higher into the TTL, as expected. Here, $D_{\max}$ is roughly tripled for a doubling of CAPE. The mean entrainment flux ratio $D_{\min}/D_{\max}$ remained close to -0.1 throughout these changes. Such behavior is typical of other entrainment layers. This entrainment flux ratio was also found to be robust to changes in the input sounding described in section 3a, although in that case slightly more CAPE developed while all indices of convective intensity decreased. This suggests that the initial presence of a low cloud layer enhanced the intensity of subsequent deep convection. The robustness of this ratio, if it holds up in more general conditions, would constitute a breakthrough in our ability to quantify the amount of convective cooling near the tropopause in the real atmosphere. However, when allowing for cloud glaciation in the model, we obtained a somewhat higher entrainment flux ratio. The role of microphysics will require further study. Also, the entrainment ratio varies somewhat during the life of the storm and, because of our experiment design, it is not possible to quantify exactly the value toward which this converges in a convective equilibrium situation. One consequence of the deepening of convection is a shallowing of the uppermost layer in which turbulent cooling takes place. The peak cooling rate (in K h^{-1}) varied as the ratio of energy removed ($D_{\min}$) to the mass of this layer. Since the former increased with CAPE, while the latter decreased, the peak cooling increased very sharply with CAPE—an order of magnitude for a doubling of CAPE. While various measures of convective intensity increased with CAPE in these experiments with all other things held equal, modest changes to the input sounding (described in section 3a) caused CAPE and intensity to shift in opposite directions. This indicates that CAPE by itself is not an adequate predictor of intensity and that other factors must be considered, which is a matter for future work.

There are still many other factors that remain to be considered in future work. Examples include the impact of changes in surface forcing, background thermal profile, and treatment of microphysics. Finally, another important factor that we have excluded is wind shear. This will cause wave braking and may affect our results. However, because of the complexity of the problem we defer this to a future publication.

Acknowledgments. We are grateful to NCAR for supercomputing resources. F. J. Robinson is grateful to Alexandre Costa for advice on this manuscript. This work was supported by NASA EOS/IDS Grant NAG-59632.

REFERENCES

Asplund, M., H.-G. Ludwig, H. Å. Nordlund, and R. Stein, 2000: The effects of numerical resolution on hydrodynamical surface convection simulations and spectral line formation. *Astron. Astrophys.,* **359,** 669–681.

Deardorff, J. W., G. E. Willis, and G. H. Stockton, 1980: Laboratory studies of the entrainment zone of a convectively mixed layer. *J. Fluid Mech.,* **100,** 41–64.

Dessler, A., 2002: The effect of deep, tropical convection on the tropical tropopause layer. *J. Geophys. Res.,* **107,** 4033, doi:10.1029/2001JD000511.

Fedorovich, E., and R. Conzemius, 2004: Convective entrainment into a shear-free, linearly stratified atmosphere: Bulk models reevaluated through large-eddy simulations. *J. Atmos. Sci.,* **61,** 281–294.

Fueglistaler, S., H. Wernli, and T. Peter, 2004: Tropical troposphere-to-stratosphere transport inferred from trajectory calculations. *J. Geophys. Res.,* **109,** D03108, doi:10.1029/2003JD004069.

Gage, K. S., J. R. McAfee, D. A. Carter, W. L. Ecklund, A. C. Riddle, G. C. Reid, and B. B. Balsley, 1991: Long-term mean vertical motion over the tropical Pacific: Wind-profiling Doppler radar measurements. *Science,* **254,** 1771–1773.

Grabowski, W. W., X. Wu, M. W. Moncrieff, and W. D. Hall, 1998: Cloud-resolving modeling of cloud systems during phase III of GATE. Part ii: Effects of resolution and the third spatial dimension. *J. Atmos. Sci.,* **55,** 3264–3282.

Hartmann, D. L., J. R. Holton, and Q. Fu, 2001: The heat balance of the tropical tropopause, cirrus, and stratospheric dehydration. *Geophys. Res. Lett.,* **28,** 1969–1972.

Holton, J., and A. Gettelman, 2001: Horizontal transport and the dehydration of the stratosphere. *Geophys. Res. Lett.,* **28,** 2799–2802.

Hong, S.-Y., H.-M. H. Juang, and Q. Zhao, 1998: Implementation of prognostic cloud scheme for a regional spectral model. *Mon. Wea. Rev.,* **126,** 2621–2639.

Kessler, E., 1969: *On the Distribution and Continuity of Water Substance in Atmospheric Circulation. Meteor. Monogr.,* No. 32, Amer. Meteor. Soc., 84 pp.

Kirk-Davidoff, D. B., E. J. Hintsa, J. Anderson, and D. W. Keith, 1999: The effect of climate change on ozone depletion through changes in stratospheric water vapour. *Nature,* **402,** 399–401.

Klemp, J., and R. Wilhelmson, 1978: The simulation of three-dimensional convective storm dynamics. *J. Atmos. Sci.,* **35,** 1070–1096.

Kuang, Z., and C. Bretherton, 2004: Convective influence on the heat balance of the tropical tropopause layer: A cloud-resolving model study. *J. Atmos. Sci.,* **61,** 2919–2927.

Küpper, C., J. Thuburn, G. Craig, and T. Birner, 2004: Mass and water transport into the tropical stratosphere: A cloud resolving simulation. *J. Geophys. Res.,* **109,** D10111, doi:10.1029/2004JD004541.

Lane, T., R. Sharman, T. Clark, and H.-M. Hsu, 2003: An investigation of turbulence generation mechanisms above deep convection. *J. Atmos. Sci.,* **60,** 1297–1321.

Larson, M., and L. Jönsson, 1995: Modeling of mixing by turbulent jet in stably stratified fluid. *J. Hydraul. Eng.,* **32,** 271–289.

Lilly, D., 1962: On the numerical simulation of buoyant convection. *Tellus,* **14,** 148–172.

Moeng, C., J. McWilliams, R. Rotunno, P. Sullivan, and J. Weil, 2004: Investigating 2D modeling of atmospheric convection in the PBL. *J. Atmos. Sci.,* **61,** 889–903.

Muthsam, H. J., W. Goeb, F. Kupka, W. Liebich, and J. Zoechling, 1995: A numerical study of compressible convection. *Astron. Astrophys.,* **293,** 127–141.

Read, W. G., D. L. Wu, J. W. Waters, and H. C. Pumphrey, 2004: Dehydration in the tropical tropopause layer: Implications from the UARS Microwave Limb Sounder. *J. Geophys. Res.,* **109,** D06110, doi:10.1029/2003JD004056.

Robinson, F., P. Demarque, L. Li, S. Sofia, Y.-C. Kim, K. Chan, and D. Guenther, 2003: 3D convection simulations of the outer layers of the sun using realistic physics. *MNRAS,* **340,** 923–936.

Sherwood, S. C., 1999: On moistening of the tropical troposphere by cirrus clouds. *J. Geophys. Res.,* **104,** 11 949–11 960.

——, 2000: A stratospheric "drain" over the maritime continent. *Geophys. Res. Lett.,* **27,** 677–680.

——, and A. E. Dessler, 2001: A model for transport across the tropical tropopause. *J. Atmos. Sci.,* **58,** 765–779.

——, T. Horinouchi, and H. A. Zeleznik, 2003: Convective impact on temperatures observed near the tropical tropopause. *J. Atmos. Sci.,* **60,** 1847–1856.

——, P. Minnis, M. McGill, and J. Chae, 2004: Underestimation of deep convective cloud tops by thermal imagery. *Geophys. Res. Lett.,* **31,** L11102, doi:10.1029/2004GL019699.

Simmons, A. J., A. Untch, C. Jakob, P. Kallberg, and P. Unden, 1999: Stratospheric water vapour and tropical tropopause temperatures in ECMWF analyses and multi-year simulations. *Quart. J. Roy. Meteor. Soc.,* **125,** 353–386.

Simpson, J., T. D. Keenan, B. Ferrier, R. H. Simpson, and G. J. Holland, 1993: Cumulus mergers in the maritime continent region. *Meteor. Atmos. Phys.,* **51,** 73–99.

Sullivan, P., C.-H. Moeng, B. Stevens, D. Lenschow, and S. Mayor, 1998: Structure of the entrainment zone capping the convective atmospheric boundary layer. *J. Atmos. Sci.,* **55,** 3042–3064.

Thuburn, J., and G. C. Craig, 2002: On the temperature structure of the tropical substratosphere. *J. Geophys. Res.,* **107,** D24017, doi:10.1029/2001JD000448.

Wicker, L., and W. Skamarock, 2002: Time splitting methods for elastic models using forward schemes. *Mon. Wea. Rev.,* **130,** 2088–2097.